Gravitational form factors and mechanical properties of the proton: Connections between distributions in 2D and 3D

Poonam Choudhary,[1,*] Bheemsehan Gurjar,[1,†] Dipankar Chakrabarti,[1,‡] and Asmita Mukherjee[2,§]
[1]*Department of Physics, Indian Institute of Technology Kanpur, Kanpur-208016, India*
[2]*Department of Physics, Indian Institute of Technology Bombay, Powai, Mumbai 400076, India*

(Received 30 June 2022; accepted 22 September 2022; published 14 October 2022)

The gravitational form factors which are obtained from the matrix elements of the energy-momentum tensor provide us information about internal distributions of mass, energy, pressure, and shear. The Druck term is the least understood among all the gravitational form factors. In a light front quark-diquark model of a proton, we investigate the Druck form factor. Using Abel transformation, we evaluate the 3D distribution in the Breit frame from the 2D light front distributions. The results are compared with other models and lattice predictions.

DOI: 10.1103/PhysRevD.106.076004

I. INTRODUCTION

Form factors are sources of information about the internal structure of hadrons. There are several form factors that give different kinds of information about the hadrons. Hadron structures are probed by electromagnetic, weak, and gravitational interactions where particles couple to the matter fields. In electromagnetic interaction, a photon couples to a matter field and the corresponding conserved electromagnetic current gives electric and magnetic charge distributions inside the hadron through form factors. The weak interaction which is mediated through $W_{\pm}$ and Z bosons provides axial and pseudoscalar form factors of the proton. The gravitational interaction between a graviton and a proton provides mass, spin, and force distribution inside the proton [1,2]. Corresponding form factors are known as gravitational form factors and are written as matrix elements of the energy-momentum tensor (EMT) [3,4]. The electromagnetic and weak properties of the proton are well known but the internal mass or energy distributions, the forces on the quarks, and the angular momentum distribution inside the proton have attracted a lot of attention only recently.

In the forward limit, the electromagnetic form factors are equivalent to electric charge and magnetic moment and the weak interaction form factors are equivalent to the axial charge and pseudoscalar coupling while gravitational interaction describes mass, spin, and D-term [5,6] in this limit. The matrix element of the EMT describes the response of the nucleon to a change in the external spacetime metric. The components of the energy-momentum tensor tell us how matter couples to the gravitational field. The gravitational form factors are accessible through hard exclusive processes like deeply virtual Compton scattering (DVCS) as the second moments of generalized parton distribution functions (GPDs) [7–10]. In [11] a connection had been established between observables from high energy experiments and from the analysis of gravitational wave events. In the standard EMT parametrization, there are three gravitational form factors (GFFs). The GFFs $A(Q^2)$, $J(Q^2)$, and $D(Q^2)$ correspond to the time-time, time-space, and space-space components of the energy-momentum tensor, respectively. At zero momentum transfer, $Q^2 = 0$, the GFFs $A(Q^2)$ and $J(Q^2)$ are constrained by proton mass and spin respectively. The D-term form factor is the new and most exciting one which is extracted through the spatial-spatial component of the energy-momentum tensor and encodes the information on shear forces and pressure distribution inside the proton [12]. It has been calculated in several models and theories in the literature. In [12] it was shown for the first time how GPDs can give information on the mechanical properties of the proton in a DVCS process, as they are extracted from the beam charge asymmetry in DVCS, while in [13,14] the JLab group reported the first determination of the pressure and shear forces on quarks inside the proton from experimental data on DVCS. The EMT form factors of the nucleon have been investigated in various approaches, for example, in lattice QCD [15–17] in chiral perturbation theory [18–21], in the chiral quark-soliton model [22,23],

*poonamch@iitk.ac.in
†gbheem@iitk.ac.in
‡dipankar@iitk.ac.in
§asmita@phy.iitb.ac.in

as well as in the Skyrme model [24,25] and in the light cone QCD sum rule framework [26].

The pressure, shear, and energy distributions are usually defined in terms of the static EM tensor in the 3D Breit frame. In relativistic field theory, one cannot localize a particle within a Compton wavelength. In other words, the three-dimensional distributions defined in the Breit frame are subject to relativistic corrections. Alternatively, for a relativistic system, one can define them in the so-called infinite momentum frame, or light front quantization, where such relativistic effects are already incorporated. In [2] the mechanical properties like pressure, shear, and energy distributions of a nucleon in two dimensions were introduced in the light front formalism, and also later were discussed in [27]. While in some models one can easily calculate the 3D distributions, in some cases, for example in the light front wave function approach, it is easier to calculate the 2D distributions. In [28] it was shown that the 2D and 3D distributions can be connected through the Abel transformation, which would make the intuitive understanding of these distributions more clear, particularly for relativistic systems like a nucleon. In a previous work [29], the GFFs and the two-dimensional pressure, shear, and energy distributions were investigated in the spectator type model motivated by AdS/QCD. In this work, we use the same model to obtain pressure, shear, and energy distributions of the nucleon in 3D using the invertible Abel transformation. The outline of the present work is as follows: In Sec. II we briefly review the light front formalism based on the light front quark-diquark model. In Sec. III we illustrate the definition of the gravitational form factors as matrix elements of the energy-momentum tensor and define the form factors in a light front quark-diquark model. Then in Sec. IV we focus on the extraction of $D(Q^2)$ using two different approaches. And in Sec. V we show the 3D Breit frame (BF) distributions which are the Abel image of the 2D light front distributions by doing the inverse Abel transformation. And finally, in Sec. VI we present the summary and conclusion.

II. LIGHT FRONT QUARK-DIQUARK MODEL

In this model, the incoming photon, carrying a high momentum interacts with one of the valence quarks inside the nucleon, and the other two valence quarks form a spectator diquark state of spin-0 (scalar diquark). Therefore the nucleon state $|P,S\rangle$ having momentum P and spin S can be represented as a two-particle Fock state. In this article we consider the quark-scalar diquark model proposed in [30]. We use the light-cone convention $x^{\pm}=x^0\pm x^3$, and choose a frame where the transverse momentum of the proton vanishes, i.e. $P\equiv(P^+,\frac{M^2}{P^+},\mathbf{0}_\perp)$, while the momentum of the quark and the diquark are $p\equiv(xP^+,\frac{p^2+|\mathbf{p}_\perp^2|}{xP^+},\mathbf{p}_\perp)$ and $P_X\equiv((1-x)P^+,P_X^-,-\mathbf{p}_\perp)$ respectively, where $x=p^+/P^+$ is the longitudinal momentum fraction of the active quark. The two particle Fock-state expansion for the state with helicity $\pm\frac{1}{2}$ is given by

$$|P;\pm\rangle=\sum_q\int\frac{dxd^2\mathbf{p}_\perp}{2(2\pi)^3\sqrt{x(1-x)}}\times\left[\psi_+^{q\pm}(x,\mathbf{p}_\perp)\left|+\frac{1}{2},0;xP^+,\mathbf{p}_\perp\right\rangle+\psi_-^{q\pm}(x,\mathbf{p}_\perp)\left|-\frac{1}{2},0;xP^+,\mathbf{p}_\perp\right\rangle\right],\tag{1}$$

where $|\lambda_q,\lambda_s;xP^+,\mathbf{p}_\perp\rangle$ represents the two particle state with a quark having spin $\lambda_q=\pm\frac{1}{2}$, momentum p, and a scalar spectator diquark with spin $\lambda_S=0$. The two particle states are normalized as

$$\langle\lambda_q',\lambda_s';x'P^+,\mathbf{p}_\perp'|\lambda_q,\lambda_s;xP^+,\mathbf{p}_\perp\rangle=\prod_{i=1}^{2}16\pi^3p_i^+\delta(p_i'^+-p_i^+)\delta^2(\mathbf{p}_{\perp i}'-\mathbf{p}_{\perp i})\delta_{\lambda_i'\lambda_i}.\tag{2}$$

Here $\psi_{\lambda_q}^{q\lambda_N}$ are the light front wave functions with nucleon helicities $\lambda_N=\pm$. The LFWFs are given by [30]

$$\begin{aligned}\psi_+^{q+}(x,\mathbf{p}_\perp)&=\varphi^{q(1)}(x,\mathbf{p}_\perp),\\ \psi_-^{q+}(x,\mathbf{p}_\perp)&=-\frac{p^1+ip^2}{xM}\varphi^{q(2)}(x,\mathbf{p}_\perp),\\ \psi_+^{q-}(x,\mathbf{p}_\perp)&=\frac{p^1-ip^2}{xM}\varphi^{q(2)}(x,\mathbf{p}_\perp),\\ \psi_-^{q-}(x,\mathbf{p}_\perp)&=\varphi^{q(1)}(x,\mathbf{p}_\perp),\end{aligned}\tag{3}$$

where $\varphi_q^{(1)}(x,\mathbf{p}_\perp)$ and $\varphi_q^{(2)}(x,\mathbf{p}_\perp)$ are the wave functions predicted by the soft-wall AdS/QCD and can be written as

$$\varphi^{q(i)}(x,\mathbf{p}_\perp)=N_q^{(i)}\frac{4\pi}{\kappa}\sqrt{\frac{\log(1/x)}{1-x}}x^{a_q^{(i)}}(1-x)^{b_q^{(i)}}\times\exp\left[-\frac{\mathbf{p}_\perp^2}{2\kappa^2}\frac{\log(1/x)}{(1-x)^2}\right],\tag{4}$$

where $\kappa=0.4$ GeV is the AdS/QCD scale parameter and the quarks are assumed to be massless [31]. The values of the model parameters a_q^i and b_q^i and the normalization constants N_q^i were fixed by fitting the nucleon electromagnetic form factors and can be found in Ref. [32]. The wave functions can be reduced to the form predicted by AdS/QCD for $a_q^i=b_q^i=0$ [33].

III. RELATIONS BETWEEN 2D LIGHT FRONT DISTRIBUTIONS AND 3D BREIT FRAME DISTRIBUTIONS

As discussed in the Introduction, in case of nucleons the total QCD EMT for the quarks and gluons can be parametrized in terms of three independent EMT form factors [3,4,8,34,35] as

$$\langle p'|\hat{\Theta}^{\mu\nu}_{\rm QCD}(0)|p\rangle = \bar{u}(p')\Big[A(t)\frac{P^\mu P^\nu}{M} + J(t)\frac{iP^{\{\mu}\sigma^{\nu\}\alpha}\Delta_\alpha}{M} + \frac{D(t)}{4M}(\Delta^\mu\Delta^\nu - \eta^{\mu\nu}\Delta^2)\Big]u(p), \tag{5}$$

where $\hat{\Theta}^{\mu\nu}_{\rm QCD}(x)$ is the symmetric EMT operator of QCD. $P = (p+p')/2, \Delta = p' - p, t = \Delta^2$, and the symmetrization operator is defined as $X_{\{\mu}Y_{\nu\}} = \frac{1}{2}(X_\mu Y_\nu + X_\nu Y_\mu)$. The GFF $J(Q^2)$ can be expressed as $J(Q^2) = 1/2(A(Q^2)+B(Q^2))$, where $A(Q^2)$ and $B(Q^2)$ are very similar to the Dirac and Pauli form factors which are obtained from the helicity nonflip and helicity flip matrix elements of the vector current. At zero momentum transfer the values of these nucleon EMT form factors (FFs) (5) provide us with the three basic characteristics of the nucleons: the mass M, the spin $J = 1/2$, and the D-term (also known as the Druck term) D(0). The mass and the spin of the nucleons are well-observed quantities. The third mechanical characteristic, the D-term, is a more subtle term, as it is related to the distribution of the internal forces inside the nucleons [12]. For the D-term, the first experimental data are available for the nucleons [13,36]. Recently in Refs. [2,27] the 2D light front pressure and shear force distributions were obtained in terms of the Druck form factor D(t) as

$$\tilde{D}(x_\perp) = \frac{1}{4P^+}\int\frac{d^2\Delta_\perp}{(2\pi)^2}D(-\Delta_\perp^2)e^{-i\Delta_\perp\cdot x_\perp}, \tag{6}$$

$$p^{(2D)}(x_\perp) = \frac{1}{2x_\perp}\frac{d}{dx_\perp}\left(x_\perp\frac{d}{dx_\perp}\tilde{D}(x_\perp)\right), \tag{7}$$

$$s^{(2D)}(x_\perp) = -x_\perp\frac{d}{dx_\perp}\left(\frac{1}{x_\perp}\frac{d}{dx_\perp}\tilde{D}(x_\perp)\right), \tag{8}$$

where $x_\perp$ is the 2D position vector in the transverse plane. Since the 2D and 3D force distributions are expressed in terms of the same Druck term form factor $D(t)$, those distributions can be related to each other. To establish the relations between 2D and 3D distributions, it is convenient to redefine the 2D pressure $\mathcal{P}(x_\perp)$ and shear force distributions $\mathcal{S}(x_\perp)$ by multiplying Eqs. (7) and (8) with the Lorentz factor $\frac{P^+}{2M}$ [2] i.e.,

$$\mathcal{S}(x_\perp) = \frac{P^+}{2M}s^{(2D)}(x_\perp), \qquad \mathcal{P}(x_\perp) = \frac{P^+}{2M}p^{(2D)}(x_\perp). \tag{9}$$

By using the Abel transformation [37,38], these 2D LF distributions can be related to the 3D distributions in the Breit frame as [28]

$$\frac{\mathcal{S}(x_\perp)}{x_\perp^2} = \int_{x_\perp}^\infty\frac{dr}{r}s(r)\frac{1}{\sqrt{r^2-x_\perp^2}}, \tag{10}$$

$$\frac{1}{2}\mathcal{S}(x_\perp) + \mathcal{P}(x_\perp) = \int_{x_\perp}^\infty\frac{dr}{r}s(r)\sqrt{r^2-x_\perp^2}. \tag{11}$$

From Eq. (10), one can see that the function $\mathcal{S}(x_\perp)/x_\perp^2$ is the Abel image of $s(r)$. The Breit frame distributions of the elastic pressure $p(r)$ and shear force $s(r)$ in 3D are obtained in terms of Druck form factor $D(t)$ (see Refs. [1,12]) as

$$p(r) = \frac{1}{6M}\frac{1}{r^2}\frac{d}{dr}r^2\frac{d}{dr}\tilde{D}(r), \qquad s(r) = -\frac{1}{4M}r\frac{d}{dr}\frac{1}{r}\frac{d}{dr}\tilde{D}(r), \tag{12}$$

where $\tilde{D}(r)$ is the 3D Fourier transform of the Druck-term, i.e.,

$$\tilde{D}(r) = \int\frac{d^3\mathbf{\Delta}}{(2\pi)^3}e^{-i\mathbf{\Delta}\cdot r}D(-\mathbf{\Delta}^2). \tag{13}$$

The relations in Eqs. (10) and (11) have the form of invertible Abel transformation [37,38]. The inverse Abel transformation (3D Breit frame distribution in terms of the 2D light front frame distributions) of the Eqs. (10) and (11) can be obtained as [28]

$$s(r) = -\frac{2}{\pi}r^2\int_r^\infty dx_\perp\frac{d}{dx_\perp}\left(\frac{\mathcal{S}(x_\perp)}{x_\perp^2}\right)\frac{1}{\sqrt{x_\perp^2-r^2}}, \tag{14}$$

$$\frac{2}{3}s(r) + p(r) = \frac{4}{\pi}\int_r^\infty\frac{dx_\perp}{x_\perp}\mathcal{S}(x_\perp)\frac{1}{\sqrt{x_\perp^2-r^2}}. \tag{15}$$

Equation (15) implies that the normal force distribution in 3D i.e., $[\frac{2}{3}s(r) + p(r)]$, is the Abel image of the light front shear force distribution $\mathcal{S}(x_\perp)$ multiplied by $\frac{4}{\pi}$. Similarly the 2D distributions for the mass/energy $\mathcal{E}^{(2D)}(x_\perp)$ and angular momentum $\rho_J^{(2D)}(x_\perp)$ are obtained by using the 2D inverse Fourier transforms of GFFs $A(t)$ and $J(t)$ [2,23,27,28,39] as

$$\mathcal{E}^{(2D)}(x_\perp) = P^+\tilde{A}(x_\perp), \qquad \rho_J^{(2D)}(x_\perp) = -\frac{1}{2}x_\perp\frac{d}{dx}\tilde{J}(x_\perp) \tag{16}$$

where $J(x_\perp)$ is the angular momentum distribution in the 2D LF frame. $\tilde{A}(x_\perp)$ and $\tilde{J}(x_\perp)$ are the 2D inverse Fourier transform of the corresponding GFFs, i.e.

$$\tilde{F}(x_\perp) = \int \frac{d^2\Delta}{(2\pi)^2} e^{-i\Delta_\perp . x_\perp} F(-\Delta_\perp^2). \tag{17}$$

Here $x_\perp$ and $\Delta_\perp$ are respectively the position and momentum vectors in the 2D plane transverse to the propagation direction of the nucleon. The mass distribution can be redefined by multiplying the Lorentz factor as [23]

$$\mathcal{E}(x_\perp) = \frac{M}{P^+}\mathcal{E}^{(2D)}(x_\perp) \quad \text{or} \quad \mathcal{E}(x_\perp) = M\tilde{A}(x_\perp). \tag{18}$$

Similarly, by using the inverse Abel transformation of Eq. (16) one can find the 3D Breit frame distributions corresponding to the 2D mass and angular momentum distributions as

$$\epsilon(r) = -\frac{1}{\pi}\int_r^\infty \frac{dx_\perp}{x_\perp}(\mathcal{E}(x_\perp))\frac{1}{\sqrt{x_\perp^2 - r^2}}, \tag{19}$$

and

$$\rho_J(r) = -\frac{2}{\pi}r^2\int_r^\infty dx_\perp \frac{d}{dx_\perp}\left(\frac{\rho_J(x_\perp)}{3x_\perp^2}\right)\frac{1}{\sqrt{x_\perp^2 - r^2}}. \tag{20}$$

After integrating $\mathcal{E}(x_\perp)$ and $\rho_J^{(2D)}(x_\perp)$ over $x_\perp$ one can get the mass and spin of the proton as

$$\int d^2x_\perp \mathcal{E}(x_\perp) = MA(0) \quad \text{and} \quad \int d^2x_\perp \rho_J^{(2D)}(x_\perp) = J(0) \tag{21}$$

where the form factors are normalized as $A(0) = 1$ and $J(0) = 1/2$.

IV. EXTRACTION OF GFFS IN LFQDQ MODEL

The form factors $A^{u+d}(Q^2)$, $B^{u+d}(Q^2)$, and $D^{u+d}(Q^2)$ in the LFQDQ model can be parametrized in terms of structure integrals as [29,40]

$$A^{u+d}(Q^2) = \mathcal{I}_1^{u+d}(Q^2), \qquad B^{u+d}(Q^2) = \mathcal{I}_2^{u+d}(Q^2) \tag{22}$$

and

$$D^{u+d}(Q^2) = -\frac{1}{Q^2}[2M^2\mathcal{I}_1^{u+d}(Q^2) - Q^2\mathcal{I}_2^{u+d}(Q^2) - \mathcal{I}_3^{u+d}(Q^2)], \tag{23}$$

where $\mathcal{I}_i^{u+d} = \mathcal{I}_i^u + \mathcal{I}_i^d$. The explicit expressions of the structure integrals $\mathcal{I}_i^q(Q^2)$ are given by [29]

$$\mathcal{I}_1^q(Q^2) = \int dx x\left[N_1^{q2}x^{2a_1^q}(1-x)^{2b_1^q+1} + N_2^{q2}x^{2a_2^q-2}(1-x)^{2b_2^q+3}\frac{1}{M^2}\left(\frac{k^2}{\log(1/x)} - \frac{Q^2}{4}\right)\right] \times \exp\left[-\frac{\log(1/x)}{k^2}\frac{Q^2}{4}\right], \tag{24}$$

$$\mathcal{I}_2^q(Q^2) = 2\int dx N_1^q N_2^q x^{a_1^q+a_2^q}(1-x)^{b_1^q+b_2^q+2} \times \exp\left[-\frac{\log(1/x)}{k^2}\frac{Q^2}{4}\right], \tag{25}$$

$$\mathcal{I}_3^q(Q^2) = 2\int dx N_1^q N_2^q x^{a_1^q+a_2^q-2}(1-x)^{b_1^q+b_2^q+2} \times \left[\frac{4(1-x)^2k^2}{\log(1/x)} + Q^2(1-x)^2 - 4m^2\right] \times \exp\left[-\frac{\log(1/x)}{k^2}\frac{Q^2}{4}\right]. \tag{26}$$

Only the quark component of EMT has been included in the above expressions. The complete analytic expression for the D-term as given above in Eq. (23) along with Eqs. (24), (25), and (26) is found to be very lengthy and not so intuitive. It turns out that the form factor $D(Q^2) \equiv D^{u+d}(Q^2)$ can be described by the multipole function as [41]

$$D(Q^2) = \frac{a}{(1+bQ^2)^c}, \tag{27}$$

where the parameters a, b, and c are given in Table I at the initial scale as well as at a higher scale. The comparison of the GFFs at $Q^2 = 0$ with the various phenomenological models, lattice QCD, and existing experimental data for the $D(0)$ and the validity for those GFFs are discussed in Ref. [29]. In Table I fitted model parameters in the first row are extracted at the model scale $\mu_0 = 0.313$ GeV, whereas the fitted parameters in the second row correspond to the scale evolution of the GPDs from initial scale $\mu_0^2 = 0.32$ GeV^2 to the final scale $\mu^2 = 4$ GeV^2. For the evolution scheme we adopt the Dokshitzer-Gribov-Lipatov-Altarelli-Parisi (DGLAP) equations [42–44] of QCD with next-to-next-to-leading order (NNLO) of the scale evolution. We have used the higher-order perturbative parton evolution

TABLE I. Fitted parameters for the fitted function $D_{\rm fit}(Q^2)$ Eq. (27) form factor. Here $D_0^{\rm fit}$ represents the form factor at model scale while $D_1^{\rm fit}$ show the evolved form factor from initial scale $\mu_0^2 = 0.32$ GeV^2 to $\mu^2 = 4$ GeV^2 in the LFQDQ model.

Parameters	a	b	c
$D_0^{\rm fit}$	−18.8359	2.2823	2.7951
$D_1^{\rm fit}$	−1.521	0.531	3.026

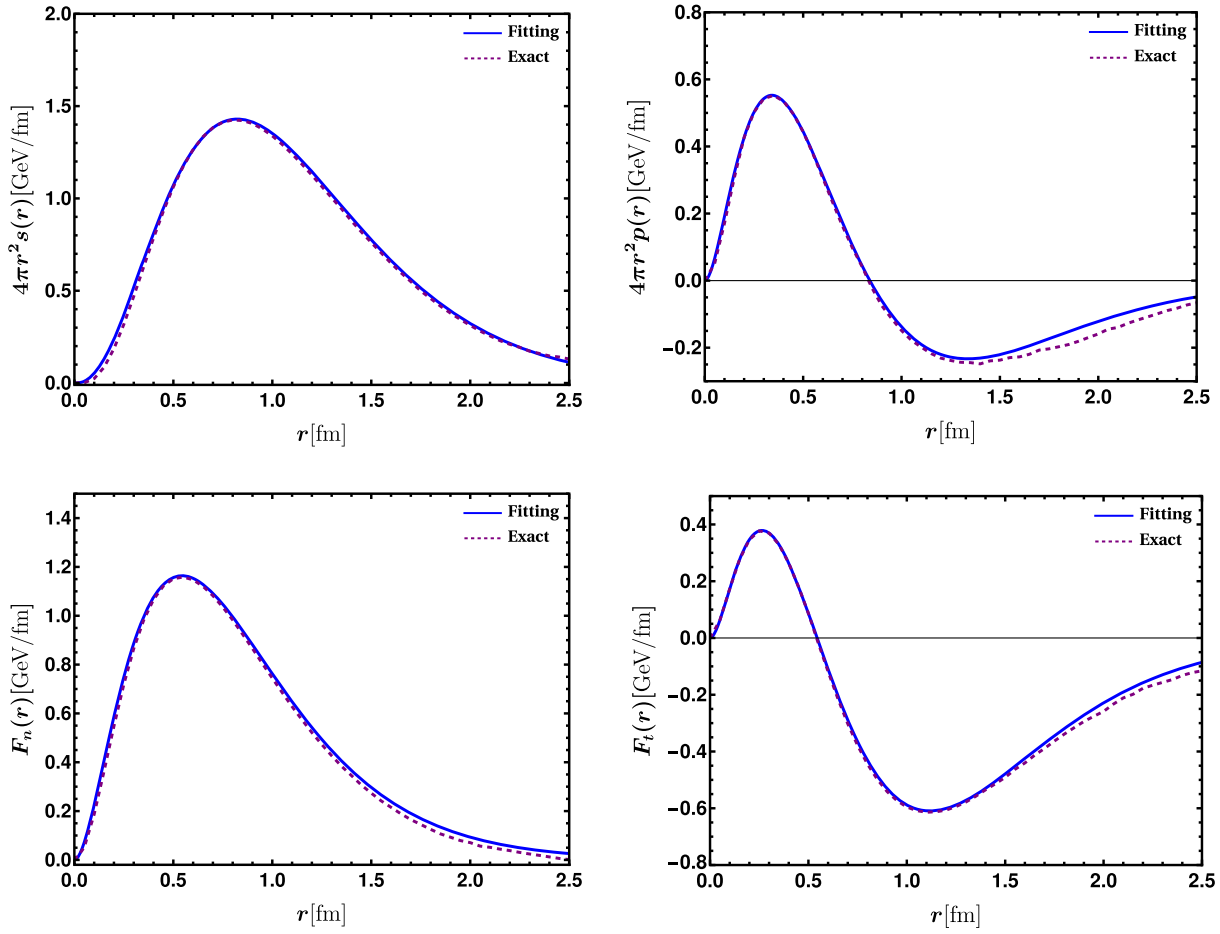

FIG. 1. The solid-blue curve in the upper left panel shows the 3D shear force distribution in the Breit frame for the LFQDQ model (using the inverse Abel transformation) at the initial scale for the fitted $D(Q^2)$ term while the purple-dashed curve is for the model data by using the Vegas. While the upper right figure draws the 3D pressure distributions. Similarly, the lower-left panel draws the 3D normal force distribution and the lower-right panel draws the 3D tangential force distribution, respectively.

toolkit (HOPPET) [45] to perform the scale evolution numerically. We find that the QCD evolution of the GFFs $A^{u+d}(Q^2)$, $B^{u+d}(Q^2)$ are consistent with the lattice QCD results [29,41]. Also the qualitative behavior of our D-term is comparable with the lattice QCD [46] and the experimental data from JLab [13] as well as other theoretical predictions from the KM15 global fit [47], dispersion relation [48], χQSM [22], Skyrme model [24], and bag model [49]. The renormalization of the QCD trace anomaly for the quark and gluon parts of the energy-momentum tensor has been studied in Ref. [50].

We have checked the accuracy of our fitting techniques at the initial scale using the multidimensional Monte Carlo integration program Vegas [51,52]. In Fig. 1 we show the 3D distributions which are computed with the fitted D-term form factor given in Eq. (27) and the exact model calculations (using Vegas) at the initial scale. From Fig 1 one can see that near the region of small spatial distance from the center of nucleon the fitted and exact model results are exactly overlapping, while for the large value of r, the distributions are slightly different in two different methods. The multipole fitting function describes the exact results very accurately for small r, but the discrepancies at large r are negligibly small. It allows us to use the multipole fitting function in place of an exact expression for evaluation of different distributions using Abel transformation.

V. DISTRIBUTIONS IN THREE DIMENSIONS

In this section, we present the results for the 3D distributions in the Breit frame (BF). The 3D BF EMT distributions are derived from the 2D LF EMT distributions by using the inverse Abel transformation [37,38].

In the left and right panels of Fig. 2, we compare the model results for the energy(mass) distributions with the chiral quark-soliton model (χQSM) [22,23] for the 2D and 3D mass distributions in the LF (Drell-Yan) and BF, respectively. By using Eq. (18) we compute the 2D momentum distributions and then the 3D momentum distributions are calculated by the inverse Abel transformation defined in Eq. (19). The values of the mass distribution in the 2D LF frame and 3D BF

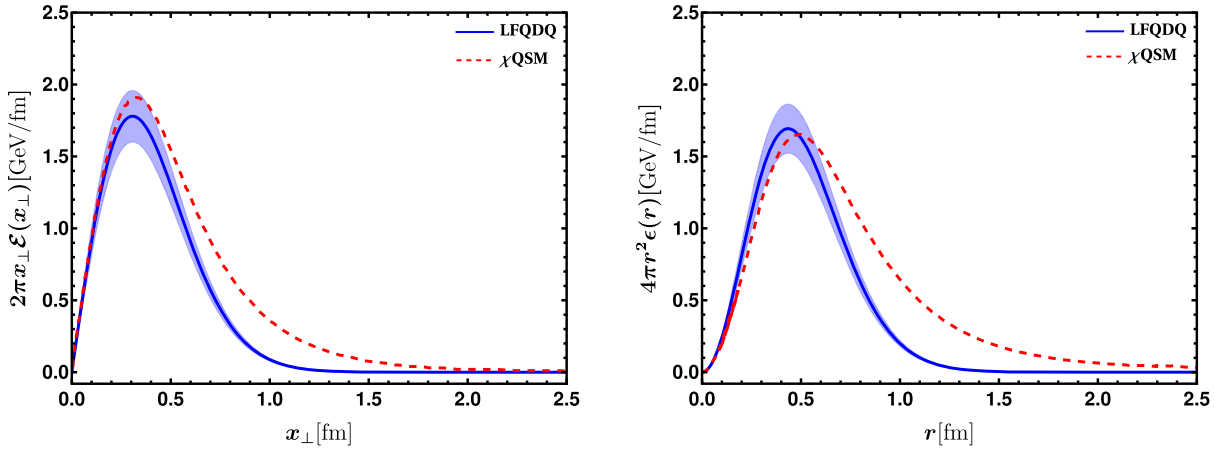

FIG. 2. The solid blue curve in the left panel shows the 2D mass distribution in the 2D LF frame for the LFQDQ model while the red-dashed curve is the 2D mass distribution for the χQSM model [23]. Similarly, the solid-blue curve in the right panel shows the 3D mass distribution in the BF for the LFQDQ (after doing the inverse Abel transformation) whereas the red-dashed curve is the 3D mass distribution for χQSM model [22]. The error bands correspond to 2% uncertainty in the model parameters and model predictions are at an evolved scale $\mu^2 = 4$ GeV^2.

at the center of the nucleon are found to be $\mathcal{E}(0) = 1.54$ GeV/fm^2 and $\epsilon(0) = 2.02$ GeV/fm^3 respectively. In Fig. 2, we have shown the 2D LF frame and 3D BF mass distributions weighted by $2\pi x_\perp$ and $4\pi r^2$ respectively. One can see from Fig. 2 that 3D mass distribution exhibits a broader shape than the 2D mass distributions. This indicates that the 3D mass radius [22] should be larger than the 2D mass radius [23]. The numerical values of the mass radii for the 2D and 3D distributions are given in Table II. The ratio between the 2D LF frame and 3D BF mean square mass radii in this model is found as

$$\frac{\langle x_\perp^2 \rangle_{\rm mass}}{\langle r^2 \rangle_{\rm mass}} = \frac{2}{3}, \tag{28}$$

where these 2D and 3D mass radii are respectively defined as [22,23,27]

$$\langle x_\perp^2 \rangle_{\rm mass} = \frac{1}{M}\int d^2x_\perp x_\perp^2 \mathcal{E}(x_\perp),$$
$$\langle r^2 \rangle_{\rm mass} = \frac{\int d^3r r^2 \epsilon(r)}{\int d^3r \epsilon(r)}. \tag{29}$$

In Fig. 3 the solid-blue curves in the left panel represent the 2D angular momentum distribution (weighted by $2\pi x_\perp$) calculated by using Eq. (16), for the LFQDQ model whereas the dashed-red curves represent the same in the χQSM model. The solid-blue (dashed-red) curves in the right panel show the 3D angular momentum distribution weighted by $4\pi r^2$ which are computed by using the inverse Abel transform given in Eq. (20), in the LFQDQ (χQSM) model. The 2D and 3D angular momentum distributions are normalized as

$$\int d^2x_\perp \rho_J^{2D}(x_\perp) = \int d^3r \rho_J(r) = J(0) = \frac{1}{2}, \tag{30}$$

which is related to the nucleon spin. Similar to the mass distribution, the 3D BF angular momentum distribution is also broader than the 2D LF frame distribution. The 2D LF frame radius [23] for the angular momentum distribution is related to the 3D BF distribution [22], and is smaller than the 3D radius by a geometric factor of 4/5, i.e.,

$$\langle x_\perp^2 \rangle_J \approx \frac{4}{5}\langle r^2 \rangle_J \tag{31}$$

TABLE II. Various observables obtained from the EMT distributions for the proton in both 2D LF and 3D BF are listed: the energy distributions at the nucleon center ($\mathcal{E}(0)$, $\epsilon(0)$), pressure distribution at the nucleon center ($\mathcal{P}(0)$, $p(0)$), nodal points of the pressure ($(x_\perp)_0$,r_0), and the mean square radii of the mass, angular momentum, and mechanical ($\langle x_\perp^2 \rangle$, $\langle r^2 \rangle$).

$\mathcal{E}(0)$ (GeV/fm^2)	$\mathcal{P}(0)$ (GeV/fm^2)	$(x_\perp)_0$ (fm)	$\langle x_\perp^2 \rangle_{\rm mass}$ (fm^2)	$\langle x_\perp^2 \rangle_J$ (fm^2)	$\langle x_\perp^2 \rangle_{\rm mech}$ (fm^2)
1.54	0.354	0.34	0.21	0.38	0.167
$\varepsilon(0)$ (GeV/fm^3)	$p(0)$ (GeV/fm^3)	r_0 (fm)	$\langle r^2 \rangle_{\rm mass}$ (fm^2)	$\langle r^2 \rangle_J$ (fm^2)	$\langle r^2 \rangle_{\rm mech}$ (fm^2)
2.02	4.76	0.43	0.32	0.51	0.251

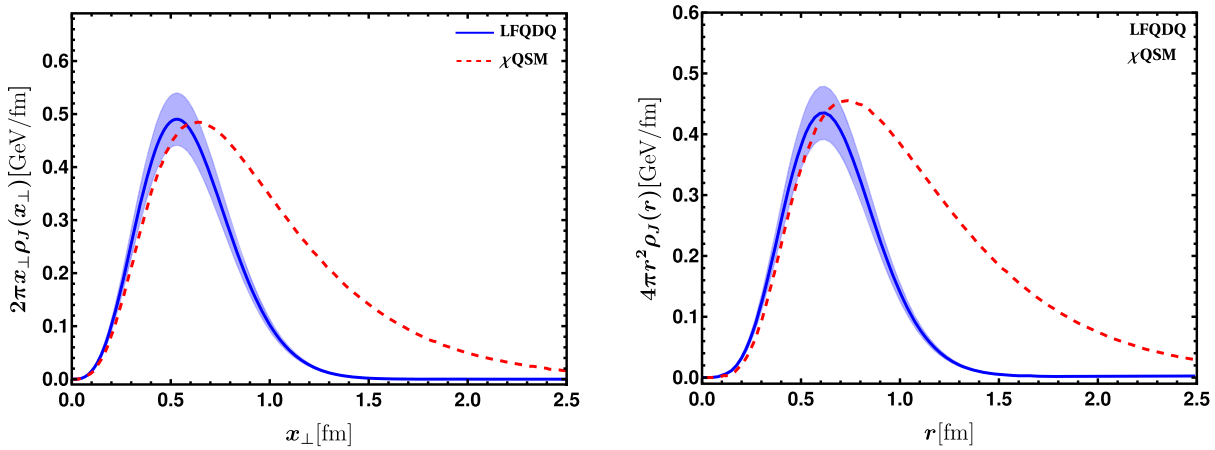

FIG. 3. The solid blue curve in the left panel shows the 2D angular momentum distribution in the LF frame for the LFQDQ model while the red-dashed curve is the 2D angular momentum distribution for the χQSM model [23]. Similarly, the solid blue curve in the right panel shows the 3D angular momentum distribution in the BF for the LFQDQ (after doing the inverse Abel transformation) whereas the red-dashed curve is the 3D angular momentum distribution for χQSM model [22]. The error bands correspond to 2% uncertainty in the model parameters and model predictions are at evolved scale $\mu^2 = 4$ GeV^2.

where these 2D LF frame and 3D BF angular momentum radii are defined as

$$\langle x_\perp^2 \rangle_J = 2 \int d^2x_\perp x_\perp^2 \rho_J^{(2D)}(x_\perp) \quad \text{and} \quad \langle r^2 \rangle_J = \frac{\int d^3r r^2 \rho_J(r)}{\int d^3r \rho_J(r)}. \tag{32}$$

The numerical values of these 2D and 3D angular momentum radii for the LFQDQ model are given in Table II.

The solid-blue curve in the left (right) panel of Fig. 4 shows the 3D pressure (shear-force) distributions for the LFQDQ model, while the black-dashed, red-dotted, and green-dot-dashed curves show the pressure and shear-force distributions for JLab, χQSM, and lattice predictions, respectively. The pressure $p(r)$ has the global maximum at $r = 0$, with $p(0) = 4.76$ GeV/fm$^3 = 7.62 \times 10^{35}$ Pa. Which is 10–100 times higher than the pressure inside a neutron star [53]. The pressure decreases monotonically, becoming zero at the nodal point, $r_0 \approx 0.43$ fm. The pressure reaches the global minimum at $r_{p,\min} = 0.67$ fm, after which it increases monotonically but remains negative until it goes to zero. The positive sign of the pressure for $r < r_0$ corresponds to the repulsion, whereas the negative sign in the region $r > r_0$ is for the attraction. Unlike pressure, the shear force distribution is always positive.

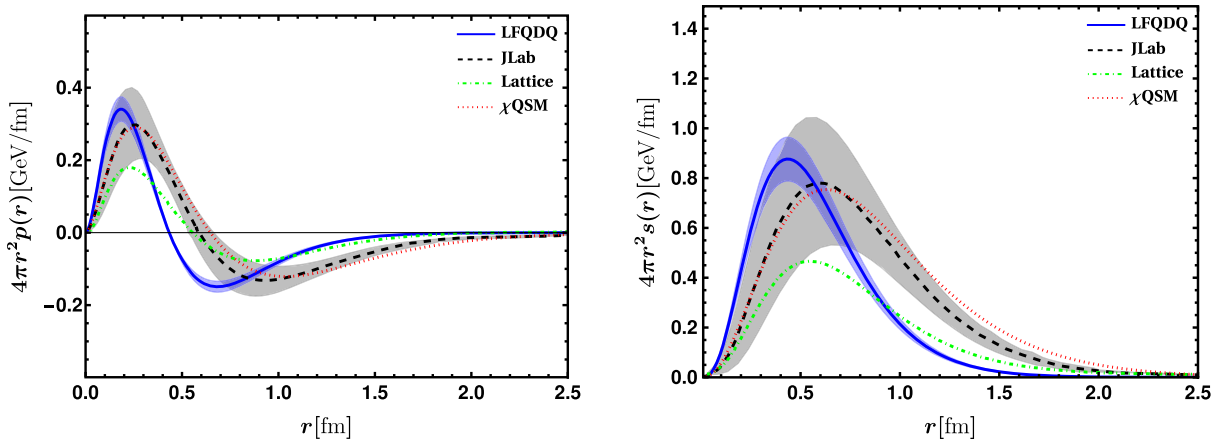

FIG. 4. The solid blue, black-dashed (with error band), red-dotted, and green-dot-dashed curves in the left panel represent the 3D pressure distributions (in Breit Frame) for LFQDQ, JLab [13,36], χQSM [22], and Lattice predictions [17], respectively. Whereas solid-blue, black-dashed, red-dotted, and green-dot-dashed curves in the right panel show the 3D shear-force distributions in the BF for LFQDQ, JLab [13,36], χQSM [22], and Lattice predictions [17]. The error bands correspond to 2% uncertainty in the model parameters and model predictions are at evolved scale $\mu^2 = 4$ GeV^2.

The conservation of the EMT currents $\partial_\mu \hat{T}^{\mu\nu} = 0$, provides the 2D as well as 3D stability conditions. We obtain the 3D equilibrium equations from the conservation of the EMT currents, which are equivalent to the 2D stable conditions as [1,23,28]

$$p'(r) + \frac{2s(r)}{r} + \frac{2}{3}s'(r) = 0$$
$$\Leftrightarrow \mathcal{P}'(x_\perp) + \frac{\mathcal{S}(x_\perp)}{x_\perp} + \frac{1}{2}\mathcal{S}'(x_\perp) = 0. \quad (33)$$

From the above Eq. (33) one can easily see that the pressure and shear forces are not independent functions but due to EMT conservation, they are related to each other. Another consequence of the EMT conservation is the von Laue condition for the 2D and 3D pressure and shear forces for the nucleons [1]

$$\int d^3 r p(r) = 0 \Leftrightarrow \int d^2 x_\perp \mathcal{P}(x_\perp) = 0, \quad (34)$$

$$\int_0^\infty dr r \left[p(r) - \frac{1}{3}s(r)\right] = 0$$
$$\Leftrightarrow \int_0^\infty dx_\perp \left[\mathcal{P}(x_\perp) - \frac{1}{2}\mathcal{S}(x_\perp)\right] = 0. \quad (35)$$

From the above two Eqs. (34) and (35) one can see that 3D von Laue conditions are satisfied if and only if the 2D ones are satisfied. By using the Eq. (33) the Druck term can be expressed in terms of 2D and 3D pressure and force distributions as

$$D(0) = -M \int d^2 x_\perp x_\perp^2 \mathcal{S}(x_\perp) = 4M \int d^2 x_\perp x_\perp^2 \mathcal{P}(x_\perp) \quad (36)$$

and

$$D(0) = -\frac{4}{15} M \int d^3 r r^2 s(r) = M \int d^3 r r^2 p(r) \quad (37)$$

respectively. It indicates that the 3D Able images of the 2D distributions show the equivalently same mechanical properties as 2D distributions.

In Refs. [1,2,54] it was shown that for the local stability of the mechanical system, the 3D and 2D pressure and shear forces should satisfy the following conditions:

$$\frac{2}{3}s(r) + p(r) > 0 \quad \text{and} \quad \frac{1}{2}\mathcal{S}(x_\perp) + \mathcal{P}(x_\perp) > 0. \quad (38)$$

These inequalities imply that the Druck term (D-term) for any stable system must be negative, i.e., $D(0) < 0$. More discussions about the local stability [Eq. (38)] can be found in Ref. [27]; it is an interesting result that the stability condition in 3D implies the stability of the 2D mechanical system [29]. This allows us to connect the 3D mechanical radius to that in 2D as

$$\langle x_\perp^2 \rangle_{\text{mech}} = \frac{4D(0)}{\int_{-\infty}^0 dt D(t)} = \frac{2}{3}\langle r^2 \rangle_{\text{mech}} \quad (39)$$

where the 2D mechanical radius is defined as

$$\langle x_\perp^2 \rangle_{\text{mech}} = \frac{\int d^2 x_\perp x_\perp^2 (\frac{1}{2}\mathcal{S}(x_\perp) + \mathcal{P}(x_\perp))}{\int d^2 x_\perp (\frac{1}{2}\mathcal{S}(x_\perp) + \mathcal{P}(x_\perp))} \quad (40)$$

and the mechanical radius in 3D is given by

$$\langle r^2 \rangle_{\text{mech}} = \frac{\int d^3 r r^2 (\frac{2}{3}s(r) + p(r))}{\int d^3 r (\frac{2}{3}s(r) + p(r))}. \quad (41)$$

Numerical verification of the stability condition Eq. (34) is presented in Fig. 5. The left panel in Fig. 5 shows $r^2 p(r)$

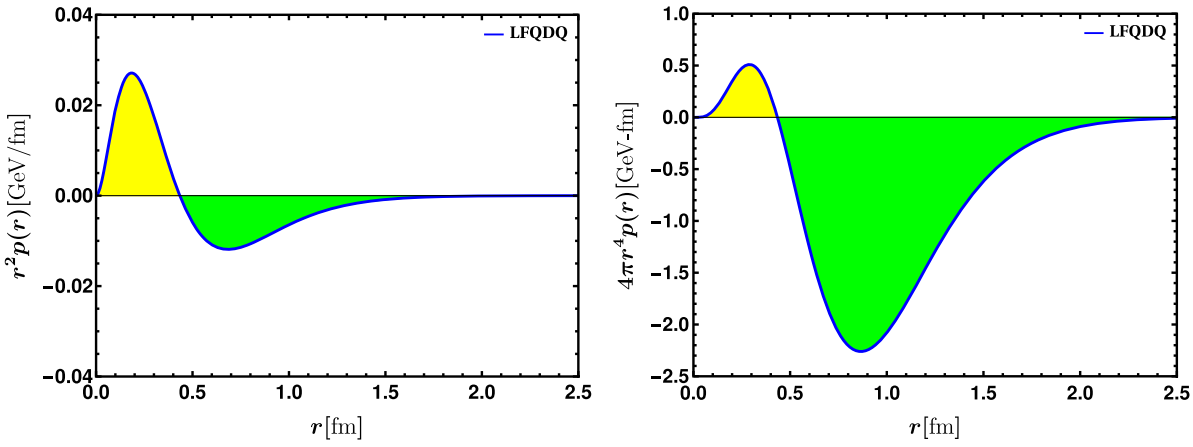

FIG. 5. Left panel shows $r^2 p(r)$ as a function of r from the LFQDQ model at evolved scale $\mu^2 = 4$ GeV^2. It shows how the stability condition $\int_0^\infty dr r^2 p(0) = 0$ in Eq. (34) is realized. Right panel shows $4\pi r^4 p(r)$. Note that the area under the curve is negative which implies $D < 0$.

as a function of r. The yellow shaded region in the positive upper half in the left panel of Fig. 5 has exactly the same surface areas as in the negative half (shaded in green). i.e.,

$$\int_0^{r_0} dr r^2 p(r) = 6.74 \text{ MeV},$$
$$\int_{r_0}^{\infty} dr r^2 p(r) = -6.74 \text{ MeV} \tag{42}$$

where r_0 is the nodal point in 3D BF, and thus they cancel each other to produce zero as required by the stability condition [Eq. (34)]. In the right panel of Fig. 5 we show $4\pi r^4 p(r)$ with r which tells us about the sign of the D-term. The area in the negative half (green) is much larger than the area in the positive half (yellow). From Eq. (37) we can see that in the LFQDQ model the D-term at zero momentum transfer takes a negative value, i.e., $D(0) < 0$. The same conclusion can be derived from Eq. (36) as well. For nucleons, the D-term is found to be negative which explains mechanical stability of the system. Note that $D(0)$ may not be negative for other systems, e.g., in Ref. [55] the D-term is found to be positive for the hydrogen atomlike system. Also in Ref. [56], it has been shown that the D-term is positive for a spin $3/2$ particle, namely the Δ resonance.

The pressure and the shear force distributions are again related to the normal (radial) and the tangential force fields, which are the eigenvalues of the stress tensor, T_{ij}. So, the 3D and the 2D force fields on the BF and the 2D LF frame can be obtained as [1,23]

$$F_n(r) = 4\pi r^2 \left[\frac{2}{3} s(r) + p(r)\right],$$
$$F_t(r) = 4\pi r^2 \left[-\frac{1}{3} s(r) + p(r)\right] \tag{43}$$

and

$$F_n^{(2D)}(x_\perp) = 2\pi x_\perp \left[\frac{1}{2}\mathcal{S}(x_\perp) + \mathcal{P}(x_\perp)\right],$$
$$F_t^{(2D)}(x_\perp) = 2\pi x_\perp \left[-\frac{1}{2}\mathcal{S}(x_\perp) + \mathcal{P}(x_\perp)\right] \tag{44}$$

respectively, In the left panel of Fig. 6 the solid-blue curve depicts the 3D normal force field, while the black-dashed, red-dotted, and the green-dot-dashed curves are the 3D normal force distributions for the JLab [13,36], χQSM [22], and lattice predictions [17], respectively. The right panel of Fig. 6 shows the 3D tangential force field distributions for the LFQDQ (solid-blue), JLab (black-dashed) [13,36], χQSM (red-dotted) [22], and lattice (green-dot-dashed) [17], respectively. The 2D normal and tangential force field distributions for the quark-scalar-diquark model can be found in Ref. [29]. In a stable spherically symmetric system the normal force $F_n(r)$ must be a stretching force otherwise the system would squeeze and collapse to the center. Whereas, the tangential force changes its direction with the distance r because the average value of possible squeezing has to be zero for a spherically symmetric system. The normal force complies with the local stability condition (38) and the tangential force satisfies the von Laue condition (34). Due to this condition, both 2D and 3D tangential forces have at least one nodal point, which tells

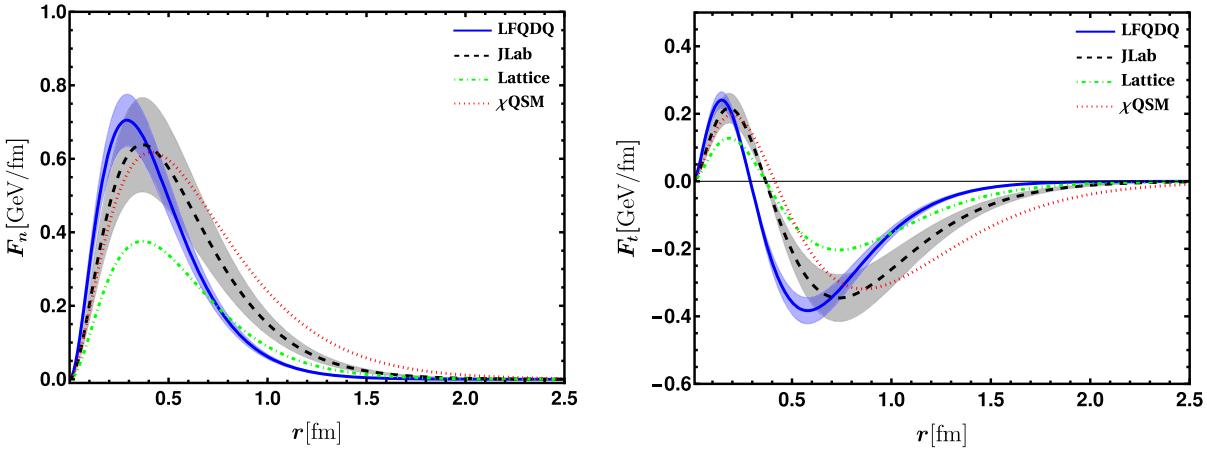

FIG. 6. The solid blue, black-dashed, red-dotted, and green-dot-dashed curves in the left panel represents the 3D normal force field distributions (in Breit frame) for LFQDQ, JLab [13,36], χQSM [22], and Lattice predictions [17], respectively. whereas the solid-blue, black-dashed, red-dotted, and green-dot-dashed curves in the right panel show the 3D tangential force field distributions in the BF for LFQDQ, JLab [13,36], χQSM [22], and lattice predictions [17], respectively. The error bands correspond to 2% uncertainty in the model parameters and model predictions are at evolved scale $\mu^2 = 4$ GeV^2.

that the direction of the force field should be reversed at this point. In the LFQDQ model the 3D and 2D tangential forces changes its direction at $r_0 \approx 0.29$ fm and $(x_\perp)_0 \approx 0.20$ fm, respectively.

In Table II, we list the numerical values for various observables such as energy and pressure densities at the center of the nucleon in both the 3D BF and 2D LF frames. The explicit values of the nodal points are also given. One can see from Table II that the magnitudes of these observables are larger in 3D BF than those in the 2D LF frame. A similar type of behavior for those observables has been also observed in Ref. [23].

VI. CONCLUSION

Of the three GFFs, Druck term, or the D-term is the least understood form factor. The D-term is physically very important as it gives the shear and pressure distributions inside the proton. Recently, JLab reported the first measurement of the shear and pressure forces inside the proton and hence there are renewed interests in recent time to study the D-term in different models. Generally, the three-dimensional distributions are defined in the Breit frame which are subject to relativistic corrections while in the light front the distributions are most conveniently evaluated in the 2D transverse plane. Recently, it was shown that the Abel transformation relates the 2D light front distributions to the 3D distributions in the Breit frame. In this paper, the 2D LF distributions are evaluated in a quark-scalar diquark model of proton and then the 3D distributions are obtained using the Abel transformation. The wave functions in the model are constructed by modifying the two-particle wave functions predicted by AdS/QCD which cannot be evaluated in perturbation theory and encode nonperturbative contributions. Our results are compared with the χQSM, JLab, and lattice predictions. The 3D stability conditions translated to 2D are found to be satisfied by the 2D distributions obtained in the LFQDQ model. Various properties, such as the energy and pressure distributions at the nucleon center, mass, angular momentum, mechanical radii, etc. are evaluated from the EMT distributions in the 2D transverse plane and the corresponding 3D distributions in the Breit frame are obtained by Abel transformations. The normal and shear force distributions are also evaluated in the LFQDQ model. Our results are found to be consistent with lattice and other model predictions.

ACKNOWLEDGMENTS

This work is supported by Science and Engineering Research Board under the Grant No. CRG/2019/000895. The work of A. M. is supported by the SERB-POWER Fellowship (No. SPF/2021/000102).

[1] M. V. Polyakov and P. Schweitzer, Int. J. Mod. Phys. A **33**, 1830025 (2018).
[2] C. Lorcé, H. Moutarde, and A. P. Trawiński, Eur. Phys. J. C **79**, 89 (2019).
[3] I. Y. Kobzarev and L. B. Okun, Zh. Eksp. Teor. Fiz. **43**, 1904 (1962), https://inspirehep.net/literature/42872.
[4] H. Pagels, Phys. Rev. **144**, 1250 (1966).
[5] M. V. Polyakov and C. Weiss, Phys. Rev. D **60**, 114017 (1999).
[6] N. Kivel, M. V. Polyakov, and M. Vanderhaeghen, Phys. Rev. D **63**, 114014 (2001).
[7] D. Müller, D. Robaschik, B. Geyer, F. M. Dittes, and J. Hořejši, Fortschr. Phys. **42**, 101 (1994).
[8] X.-D. Ji, Phys. Rev. Lett. **78**, 610 (1997).
[9] A. V. Radyushkin, Phys. Lett. B **380**, 417 (1996).
[10] A. V. Radyushkin, Phys. Lett. B **385**, 333 (1996).
[11] A. Rajan, T. Gorda, S. Liuti, and K. Yagi, arXiv:1812.01479.
[12] M. V. Polyakov, Phys. Lett. B **555**, 57 (2003).
[13] V. D. Burkert, L. Elouadrhiri, and F. X. Girod, Nature (London) **557**, 396 (2018).
[14] V. D. Burkert, L. Elouadrhiri, and F. X. Girod, arXiv:2104.02031.
[15] M. Gockeler, R. Horsley, D. Pleiter, P. E. L. Rakow, A. Schafer, G. Schierholz, and W. Schroers (QCDSF Collaboration), Phys. Rev. Lett. **92**, 042002 (2004).
[16] P. Hagler, J. W. Negele, D. B. Renner, W. Schroers, T. Lippert, and K. Schilling (LHPC, SESAM Collaborations), Phys. Rev. D **68**, 034505 (2003).
[17] P. E. Shanahan and W. Detmold, Phys. Rev. Lett. **122**, 072003 (2019).
[18] M. Dorati, T. A. Gail, and T. R. Hemmert, Nucl. Phys. **A798**, 96 (2008).
[19] J.-W. Chen and X.-d. Ji, Phys. Rev. Lett. **88**, 052003 (2002).
[20] A. V. Belitsky and X. Ji, Phys. Lett. B **538**, 289 (2002).
[21] M. Diehl, A. Manashov, and A. Schafer, Eur. Phys. J. A **31**, 335 (2007).
[22] K. Goeke, J. Grabis, J. Ossmann, M. V. Polyakov, P. Schweitzer, A. Silva, and D. Urbano, Phys. Rev. D **75**, 094021 (2007).
[23] J.-Y. Kim and H.-C. Kim, Phys. Rev. D **104**, 074019 (2021).
[24] C. Cebulla, K. Goeke, J. Ossmann, and P. Schweitzer, Nucl. Phys. **A794**, 87 (2007).
[25] H.-C. Kim, P. Schweitzer, and U. Yakhshiev, Phys. Lett. B **718**, 625 (2012).
[26] K. Azizi and U. Özdem, Eur. Phys. J. C **80**, 104 (2020).
[27] A. Freese and G. A. Miller, Phys. Rev. D **103**, 094023 (2021).
[28] J. Y. Panteleeva and M. V. Polyakov, Phys. Rev. D **104**, 014008 (2021).

[29] D. Chakrabarti, C. Mondal, A. Mukherjee, S. Nair, and X. Zhao, Phys. Rev. D **102**, 113011 (2020).
[30] T. Gutsche, V. E. Lyubovitskij, I. Schmidt, and A. Vega, Phys. Rev. D **89**, 054033 (2014); **92**, 019902(E) (2015).
[31] S. J. Brodsky and S. Gardner, Phys. Lett. B **643**, 22 (2006).
[32] D. Chakrabarti and C. Mondal, Phys. Rev. D **92**, 074012 (2015).
[33] G. F. de Teramond and S. J. Brodsky, arXiv:1203.4025.
[34] X. Ji, X. Xiong, and F. Yuan, Phys. Lett. B **717**, 214 (2012).
[35] A. Harindranath, R. Kundu, and A. Mukherjee, Phys. Lett. B **728**, 63 (2014).
[36] K. Kumerički, Nature (London) **570**, E1 (2019).
[37] M. V. Polyakov, Phys. Lett. B **659**, 542 (2008).
[38] A. M. Moiseeva and M. V. Polyakov, Nucl. Phys. **B832**, 241 (2010).
[39] C. Lorcé, L. Mantovani, and B. Pasquini, Phys. Lett. B **776**, 38 (2018).
[40] D. Chakrabarti, C. Mondal, and A. Mukherjee, Phys. Rev. D **91**, 114026 (2015).
[41] D. Chakrabarti, C. Mondal, A. Mukherjee, S. Nair, and X. Zhao, SciPost Phys. Proc. **8**, 113 (2022).
[42] Y. L. Dokshitzer, Sov. Phys. JETP **46**, 641 (1977), https://inspirehep.net/literature/126153.
[43] V. N. Gribov and L. N. Lipatov, Sov. J. Nucl. Phys. **15**, 438 (1972), https://inspirehep.net/literature/73449.
[44] G. Altarelli and G. Parisi, Nucl. Phys. **B126**, 298 (1977).
[45] G. P. Salam and J. Rojo, Comput. Phys. Commun. **180**, 120 (2009).
[46] P. Hagler *et al.* (LHPC Collaboration), Phys. Rev. D **77**, 094502 (2008).
[47] K. Kumerički and D. Müller, EPJ Web Conf. **112**, 01012 (2016).
[48] B. Pasquini, M. V. Polyakov, and M. Vanderhaeghen, Phys. Lett. B **739**, 133 (2014).
[49] X.-D. Ji, W. Melnitchouk, and X. Song, Phys. Rev. D **56**, 5511 (1997).
[50] Y. Hatta, A. Rajan, and K. Tanaka, J. High Energy Phys. 12 (2018) 008.
[51] G. P. Lepage, J. Comput. Phys. **27**, 192 (1978).
[52] G. P. Lepage, J. Comput. Phys. **439**, 110386 (2021).
[53] M. Prakash, J. M. Lattimer, J. A. Pons, A. W. Steiner, and S. Reddy, Lect. Notes Phys. **578**, 364 (2001).
[54] I. A. Perevalova, M. V. Polyakov, and P. Schweitzer, Phys. Rev. D **94**, 054024 (2016).
[55] X. Ji and Y. Liu, Phys. Rev. D **106**, 034028 (2022).
[56] D. Fu, B.-D. Sun, and Y. Dong, Phys. Rev. D **105**, 096002 (2022).